A Method for Retrieving Maize Fractional Vegetation Cover by Combining 3-D Radiative Transfer Model and Transfer Learning

Zhuo Wu, Xingming Zheng, *Member, IEEE*, Yanling Ding, *Member, IEEE*, Zui Tao, Yuan Sun, Bingze Li, Xinmeng Chen, Jianing Zhao, Yirui Liu, Xinyu Chen, and Xinbiao Li

***Abstract*—Fractional vegetation cover (FVC) is an essential parameter of vegetation canopy. Understanding its dynamics is vital for agricultural monitoring and climate change response. The physically based method for retrieving FVC from remote sensing data has great potential due to the theoretical basis of the radiative transfer model (RTM). However, the method is limited when applied to satellite imagery due to its uncertainty in simulating canopy reflectance. This article proposes a method that combines three-dimensional (3-D) RTM and convolutional neural network based transfer learning (CNN–TL) to address the inconsistency between simulated and satellite reflectance, improving maize FVC retrieval accuracy. First, 3-D RTM was employed to generate canopy reflectance datasets of maize at various growth stages. Second, CNN–TL is used to eliminate the discrepancy between 3-D RTM simulated reflectance and satellite reflectance, and the retrieval accuracy of CNN–TL is compared with random forest regression (RF) and CNN. Finally, the feasibility of the method was validated using time-series of measured data from multiple samples covering different growth stages of maize from 2021 to 2023. The results showed that, when retrieving maize FVC on GF-1, HJ-2, and Sentinel-2, CNN–TL performed the best (RMSE = 0.117, 0.063, and 0.081) compared to RF (RMSE = 0.186, 0.226, and 0.184) and CNN (RMSE = 0.133, 0.117, and 0.098). The spatial distribution of FVC maps remains highly consistent across all three satellites, indicating the exceptional performance of CNN–TL. These results contribute to the development of physically based methods for FVC retrieval and serve as a reference for multisource satellite studies.**

Received 20 May 2024; revised 31 July 2024; accepted 21 August 2024. Date of publication 26 August 2024; date of current version 13 September 2024. This work was supported in part by the National Natural Science Foundation of China under Grant 42271333, in part by the Natural Science Foundation of Jilin Province (the central government guides local science and technology development funds) under Grant YDZJ202201ZYTS484, in part by the Common Application Support Platform for National Civil Space Infrastructure Land Observation Satellites under Grant 2017-000052-73-01-001735, in part by the Fundamental Research Funds for the Central Universities under Grant 2412022ZD027, and in part by the Strategic Priority Research Program of the Chinese Academy of Sciences under Grant XDA28070500. *(Corresponding author: Yanling Ding.)*

Zhuo Wu, Yanling Ding, Xinmeng Chen, Jianing Zhao, and Yirui Liu are with the School of Geographical Sciences, Northeast Normal University, Changchun 130024, China (e-mail: wuzhuo@nenu.edu.cn; dingyl720@nenu.edu.cn; chenxm997@nenu.edu.cn; jnzhao@nenu.edu.cn; liuyirui@nenu.edu.cn).

Xingming Zheng, Bingze Li, Xinyu Chen, and Xinbiao Li are with the State Key Laboratory of Black Soils Conservation and Utilization, Northeast Institute of Geography and Agroecology, Chinese Academy of Sciences, Changchun 130102, China (e-mail: zhengxingming@iga.ac.cn; libingze@iga.ac.cn; chenxinyu@student.jlju.edu.cn; lixinbiao@iga.ac.cn).

Zui Tao and Yuan Sun are with the Aerospace Information Research Institute, Chinese Academy of Sciences, Beijing 100094, China (e-mail: taozui@aircas.ac.cn; sunyuan@aircas.ac.cn).

Digital Object Identifier 10.1109/JSTARS.2024.3450301

***Index Terms*—Convolutional neural network (CNN), fractional vegetation cover (FVC), multispectral remote sensing, three-dimensional radiative transfer model (3-D RTM), transfer learning (TL).**

I. Introduction

CROPS play a significant role in the Earth's ecosystems and the worldwide food supply chain, and monitoring their growth processes in real time is not only essential for high yields and sustainable agriculture, but it improves farmland and global ecosystems stability [1], [2]. Fractional vegetation cover (FVC) is defined as the vertically projected area of green vegetation elements (including leaves, stems, and branches) per unit of horizontal ground surface area [3]. It is a biophysical parameter that affects crop morphology and physiological features [4]. Hence, it is the key trait of interest for characterizing crop growth status and yield and is essential for crop-growth modeling [5]. The FVC is also a fundamental parameter in modeling agricultural carbon dynamics and ecosystem health [6], [7], [8]. Accurate estimation of crop FVC is of great scientific and practical importance.

Satellite remote sensing has the ability of long time series and repeated observation, making it the most effective way to estimate FVC at regional or global scale [9]. Methods for retrieving FVC from remote sensing data mainly include pixel unmixing models, empirical regression models, and physical-based model [10]. Among them, the pixel unmixing models assume that each pixel is composed of several components and consider the proportion of vegetation components as the FVC of the pixel [11], [12]. This kind of methods face challenges in determining the endmembers and extracting pure endmembers of different components [13], [14]. Empirical regression methods focus on establishing the relationship between field-measured FVC and the reflectance of specific bands or vegetation indices (VIs) [15]. The commonly used VIs include normalized difference vegetation index (NDVI), the enhanced VI, soil-adjusted vegetation index, and so on. Due to the ability to mitigate the natural collinearity and efficiency of many machine-learning (ML) methods, regression based on ML is quite popular within the crop breeding and precision agriculture community. Numerous studies have explored artificial neural networks, random forest (RF), Gaussian process regression, and partial least squares to estimate FVC [16], [17], [18]. However, the performance of regression-based approaches is constrained by the quantify,

representativeness, and quality of ground truth datasets [19], which limit their spatial and temporal generalizability [20]. Recent advancement in computer vision techniques, deep-learning approaches, such as convolutional neural networks (CNNs), can extract the deep features of input images and have been utilized to estimate crop parameters with excellent performance [21], [22].

Physical-based models, on the other hand, use the inversion of radiative transfer model (RTM) based simulation to estimate crop biophysical attributes [23], [24]. The RTM simulates canopy reflectance under different leaf and canopy attributes and backgrounds. This approach does not require any field measurements for calibration, despite sometimes using them as prior knowledge to define the parameters of RTM. To accurately describe the interaction of sunlight with vegetation canopies and other objects in the environment, researchers have developed different RTMs, such as PROSAIL [25], DART [26], RAPID [27], and LESS [28]. For crop biophysical trait estimation, PROSAIL is one of the most popular models, which is a one-dimensional (1-D) bidirectional model that assumes that the canopy is a turbid medium in which leaves as absorbing and scattering particles are small and randomly distributed in space. The canopy characteristics of continuous crops are close to this assumption [29], hence PROSAIL is widely used to simulate the reflectance of homogeneous canopy [30]. Nonetheless, 3-D RTMs simulate canopy reflectance based on a more realistic 3-D canopy structure description, providing relatively high simulating accuracy [31]. Maize is usually sowed in the row mode, which means that crops are separated by bare soil across the rows during the early growing season. With the growth of maize, the row canopy trends to be homogeneous. A 3-D RTM which can simulate the changes in maize canopy across the growth stages is expected to improve the retrieval accuracy of FVC.

ML methods and deep learnings are also widely used for indirect inversion FVC from RTM models [32]. However, the challenge of RTM inversion is its "ill-posed" problem, where various combinations of canopy biophysical variables may produce similar canopy reflectance. On the other side, due to sensor signal-to-noise ratios and spectral noise, atmospheric conditions, and other factors, there are always discrepancies between simulated and satellite measured reflectance [33]. The key to improving FVC retrieval accuracy from RTM is to find the optimal match between the simulated and the actual reflectance. To mitigate this challenge, recent studies focused on transfer learning (TL), which enables users to train a new deep-learning network with RTM simulation dataset and fine-tuned with field data. The integration of RTM simulation and ground truth data through TL can incorporate domain knowledge on RTM, mitigate spectral input noises, reduce the demand for field data, and therefore potentially achieve high model accuracy [34], [35]. TL can be stated to leverage the strengths of both regression-based methods and physical-based approaches, which is highly needed and deserves exploration.

The general objective of this article is to develop a method based on a 3-D RTM and TL-based CNN aiming at estimating maize FVC from Sentinel-2, GF-1, and HJ-2 satellites, respectively. The rest of this article is organized as follows. Section II introduces an overview of the study area, the field dataset, and three satellites data. The strategy for simulating maize canopy across the growth stages using LESS model and the TL-based CNN method for FVC estimation are also described in Section II. The evaluation of TL-based CNN to quantify FVC compared to conventional ML (i.e., RF) trained by field data and the comparison of FVC retrieval results from Sentinel-2, GF-1, and HJ-2 are presented in Section III. The potential of LESS model for maize FVC retrieval, the advantages of TL, and the performance of three satellites are discussed in Section IV. Finally, Section V concludes this article.

TABLE I
INFORMATION ON THE FIELD EXPERIMENT DATES AND SATELLITE TRANSIT

Year	Date	Maize growth stage	Sample size	Sentinel-2	GF-1	HJ-2
2021	06/22-06/26	V6-Sixth-Leaf	12	06/23	06/22	-
	07/15-07/18	V12-Twelfth-Leaf	12	07/13	07/13	07/20
	08/21-08/25	R3-Milk	13	08/22	08/19	08/24
2022	06/03-06/09	V4-Fourth-Leaf	19	06/08	06/11	06/10
	06/29-07/03	V10-Tenth-Leaf	17	07/06	06/27	-
	08/07-08/13	R2-Blister	19	08/10	08/03	-
2023	06/19-06/23	V6-Sixth-Leaf	24	06/18	06/19	06/19
	07/07-07/12	V12-Twelfth-Leaf	28	07/08	07/09	07/12

II. MATERIALS AND METHODS

A. Study Area and Field Measurements

The study area is located in Youyi County, Heilongjiang Province, China (46°45′N, 131°55′E) (Fig. 1). It has a temperate monsoon climate, with an annual average temperature of 2.5°C and an average annual precipitation of 476.5 mm. Maize is planted in May and harvesting begins in early October in the study area. Eight timestamps were selected (DOY 154–160, DOY 170–174, DOY 173–177, DOY 180–185, DOY 188–192, DOY 196–199, DOY 219–226, and DOY 233–237) for field data collection in order to capture the dynamics of maize FVC between 2021 and 2023. The dates of the field experiments as well as the growth stages of maize are shown in Table I.

Plot sizes of 30 m × 30 m were considered and divided into 3 × 3 grids with each grid of 10 m × 10 m. Three grids in the diagonal direction were selected and three sampling points in each grid were selected for measuring crop traits. Maize height, planting density, FVC photos, latitude, and longitude were collected in each sample point (Fig. 2). Photos above the maize canopy were collected vertically downward using the camera of the DJI Air 2S UAV. The flight height is 6 m, resulting in photos at least covering eight ridges with pixel size of 5472 × 3078. The photos were then clipped to preserve only the central portion with a size of 2400 × 2400 pixels.

A random forest classification (RFC) algorithm was used to extract FVC by classifying UAV-derived RGB images. The UAV images were classified into two categories: vegetation and soil. The FVC is calculated as the number of pixels in the vegetation class divided by the total number of pixels in an image. There are 1600 training samples that were generated to construct an RFC model. Of these, 70% were used for training and the remaining were used for evaluation. The classification had a high accuracy. The overall accuracy was about 0.99. The producer's accuracy

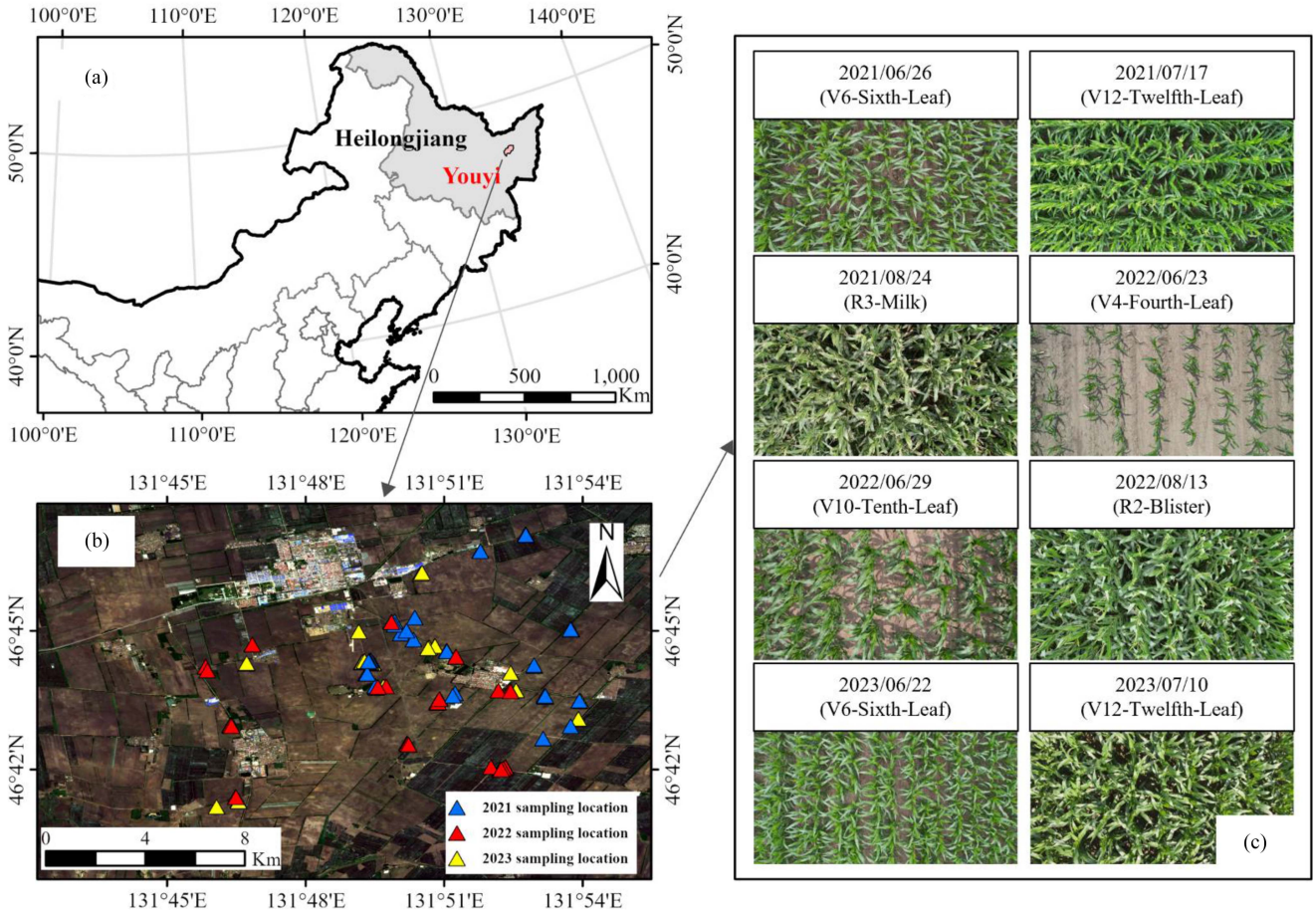

Fig. 1. (a) Study area and location of ground measurements. (b) Location of experimental sites in the Youyi County. (c) Part of field photos.

for the vegetation class was 0.99. Additionally, 26 photos were chosen for visual assessment to evaluate the accuracy of the RFC model. The R^2 value was 0.99, and the RMSE was 0.013 (Fig. 2), indicating that the RFC accurately extracted FVC. In total, 1260 maize FVC photos were collected in the field experiments.

B. Satellite Data

GF-1 and HJ-2 were launched from China in April 2013 and September 2020, respectively. The GF-1 WFV sensor is available in four bands, covering the spectral range from the visible to the near infrared (NIR). The HJ-2 CCD sensor is available in five bands, with an additional red-edge band that captures crop-specific spectral characteristics. Both GF-1 WFV sensors and HJ-2 CCD sensors have a spatial resolution of 16 m, but with different band ranges [36], [37]. The GF-1 and HJ-2 images were downloaded from the China Resources Satellite Data and Application Center (CRESDA, http://www.cresda.com). The radiance was converted to top of atmosphere reflectance using calibration coefficients provided by CRESDA. The FLAASH module in the ENVI 5.2 software was used for atmospheric correction. The Sentinel-2 L2A level image was used as the reference image to precise geometric correction of the GF-1 and HJ-2 images to ensure that the spatial deviation is less than 0.5 pixels.

Sentinel-2 consists of two satellites, namely Sentinel-2A and Sentinel-2B, which were launched by the European Space Agency in June 2015 and March 2017. The multispectral imager equipped with Sentinel-2 provides 13 bands including visible, red-edge, NIR, and shortwave infrared bands [38]. The level 2A product of bottom-of-atmosphere reflectance was acquired from the Google Earth engine. The data were resampled using the SNAP application to a 10-m resolution (https://step.esa.int/main/download/snapdownload/).

To estimate FVC, cloud-free scenes from GF-1, HJ-2, and Sentinel-2 that were as near to the field experiments as possible were selected. Table II provides comprehensive details about the satellite images that were employed.

C. Simulating Dataset Generation Using LESS

The LESS model is a newly proposed ray-tracing-based 3-D RTM which employs a weighted forward photon tracing method to simulate scene spectral reflectance [28]. Previous articles have simulated different canopies using LESS, such as apple tree orchards and grasslands [39], [40].

The essential inputs of the LESS model are the 3-D structure (e.g., crop plant), component spectrum (e.g., leaf reflectance and soil background reflectance), observation geometry, and scene illumination parameters (e.g., sky light proportion).

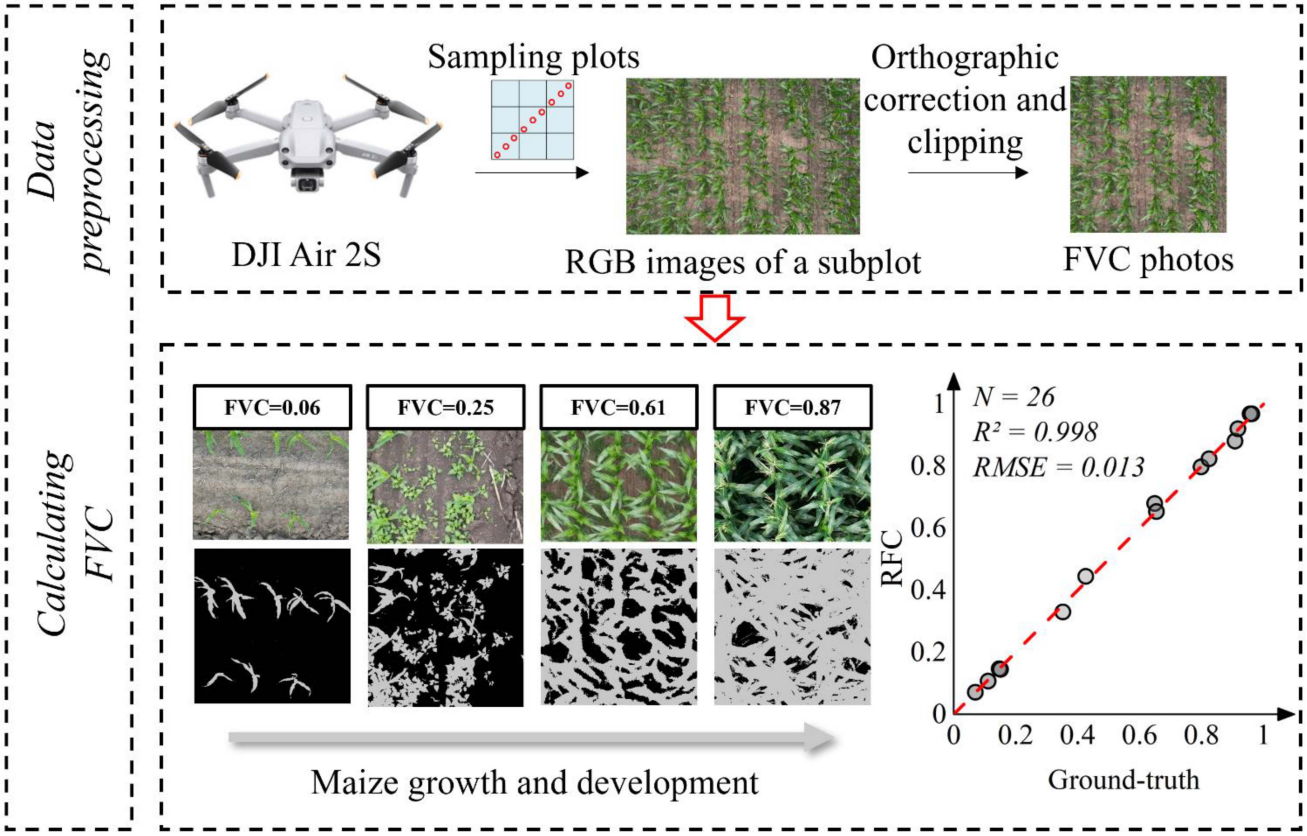

Fig. 2. FVC extraction flowchart.

TABLE II
GF-1/WFV, HJ-2/CCD, AND SENTINEL-2/MSI BANDS

Payloads	Bands	Central Wavelength (μm)	Spatial resolution (m)
WFV	**1-Blue**	**0.485**	**16**
	2-Green	**0.555**	**16**
	3-Red	**0.660**	**16**
	4-NIR	**0.830**	**16**
CCD	**1-Blue**	**0.485**	**16**
	2-Green	**0.555**	**16**
	3-Red	**0.660**	**16**
	4-NIR	**0.830**	**16**
	5-Vegetation red-edge (RE)	**0.710**	**16**
MSI	1-Ultra blue (coastal/aerosol)	0.443	60
	2-Blue	**0.490**	**10**
	3-Green	**0.560**	**10**
	4-Red	**0.665**	**10**
	5-Vegetation red-edge (RE1)	**0.705**	**20**
	6-Vegetation red-edge (RE2)	0.740	20
	7-Vegetation red-edge (RE3)	0.783	20
	8-NIR	**0.842**	**10**
	8A-Narrow NIR	0.865	20
	9-Water vapor	0.945	60
	10-Cirrus	1.375	60
	11-Shortwave infrared 1	1.610	20
	12-Shortwave infrared 2	2.190	20

Bands used are indicated in bold.

The 3-D models for maize plants with different leaves and heights came from the LESS model, but were modified by 3ds MAX 2015 software using the field measurements, such as plant height, leaf length and width, and number of leaves.

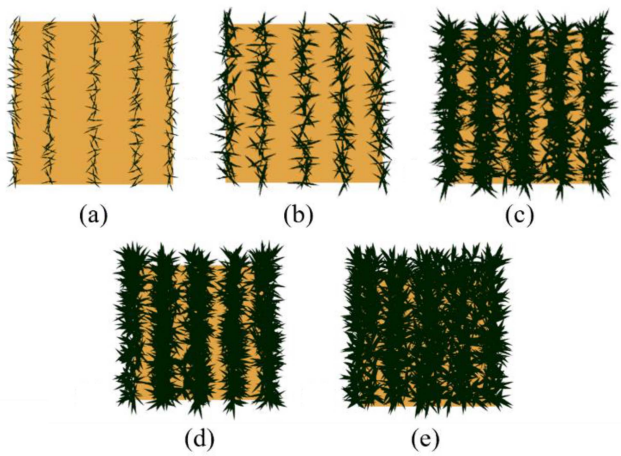

Fig. 3. 3-D maize scenes with different FVC levels: (a) FVC = 0.1, (b) FVC = 0.3, (c) FVC = 0.5, (d) FVC = 0.7, and (e) FVC = 0.9. They are all in row distribution.

The simulated scenes are covered by maize plants in row structure with spacing determined from field measurements. It could make the simulated canopy closest to the actual situation (Fig. 3). The range of FVC truth designed in LESS was 0.05–0.95 with an increment of 0.05. The component (i.e., leaf) spectra was simulated by the PROSPECT-D model [41]. The input parameters of the PROSPECT-D model are listed in Table III with reference of the knowledge of the biophysical

TABLE III
NOMINAL VALUE RANGES OF PARAMETERS USED FOR LESS AND PROSPECT-D

	RTM parameters	Symbol [unit]	Fixed value or range
Canopy parameters (LESS)	FVC	Unitless	0.05—0.95(step:0.05)
	Bands	[nm]	400—1000(step:1)
	Observation location	(Azimuth, Zenith) [°]	0, 0
	Sun location	(Azimuth, Zenith) [°]	160—170, 25-55
Leaf parameters (PROSPECT-D)	N	Unitless	1—2(step:0.5)
	Chlorophyll content	Cab [μg/cm^2]	20—90(step:5)
	Equivalent water thickness	Cw [Cm]	0.015—0.03(step:0.015)
	Dry matter content	Cm [g/cm^2]	0.004—0.01(step:0.003)

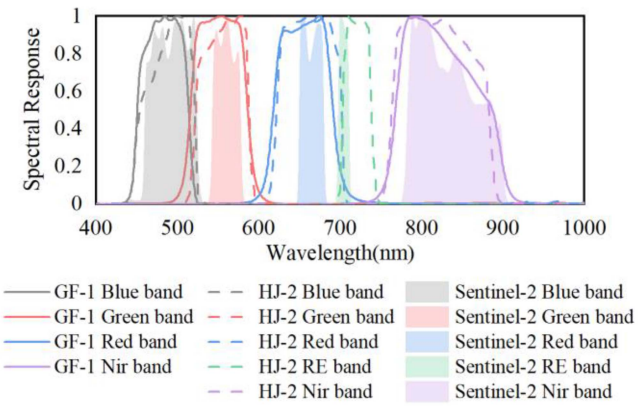

Fig. 4. Spectral response functions used in this article. The solid, delineated, and unframed curves are the spectral response functions of the GF-1, HJ-2, and Sentinel-2 sensors, respectively; black, red, blue, green, and violet represent the blue, green, red, red-edge, and near infrared spectral bands, respectively.

conditions of maize in the study area, Leaf Optical Properties Experiment, and relevant literature reviews [15], [24], [42]. In addition, the soil reflectance was measured using SEI SR-8800 in the field. The sun-sensor geometry was determined based on satellite metadata and the geographic location of the study area. The simulated dataset includes 15 391 reflectance from 400 to 1000 nm with 1-nm wavelength intervals. The simulated reflectance was resampled based on the spectral response functions (SRF) of GF-1, HJ-2, and Sentinel-2 (Fig. 4).

D. FVC Retrieval Algorithm

The simulation datasets generated by LESS were used to develop FVC retrieval models, and the performance of LESS combined with CNN–TL on different satellites was evaluated by comparing with CNN and RF. The LESS-simulated dataset consisting of VIs calculated from the resampled reflectance and the corresponding FVC. The ground measurement dataset (GD) consists of three satellite actual reflectance and measured FVC. Table IV shows the details of the datasets used for each model.

1) VIs Used to Retrieve FVC: To mitigate the impact of mixing effects and alleviate shadowing effects arising from the

TABLE IV
DATASETS USED FOR DIFFERENT MODELS

Model	Training (data size)	Transfer learning (data size)	Validation (data size)
CNN	LD (n = 12 313)		GD (n (GF1) = 86, n (HJ2) = 61, n (Sentinel2) = 45)
CNN–TL (TL)	LD (n = 12 313)	GD (n (GF1) = 58, n (HJ2) = 40, n (Sentinel2) = 30)	GD (n (GF1) = 86, n (HJ2) = 61, n (Sentinel2) = 45)
RF	LD (n = 12 313)		GD (n (GF1) = 86, n (HJ2) = 61, n (Sentinel2) = 45)

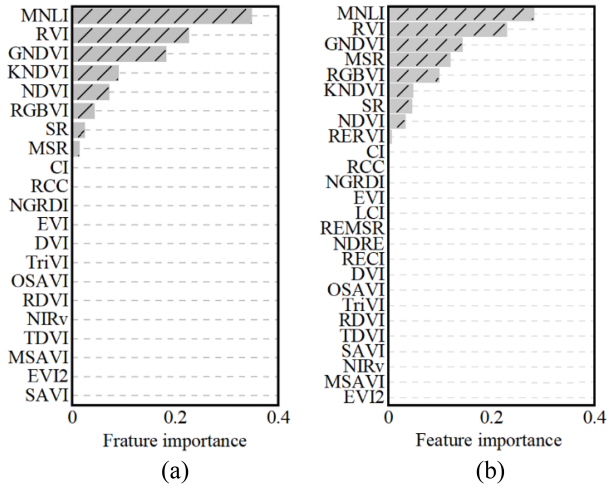

Fig. 5. Contribution of the two sets of VIs to the FVC retrieval model: (a) 21 conventional VIs and (b) 26 VIs including 21 conventional VIs and 5 red-edge VIs.

complex structure of the real world, as well as variations in sun-sensor geometry. VIs were usually used for FVC estimation [43]. Single indices may not be enough to capture the range of crop variations because of the complex interplay of canopy structure, leaf properties, and soil properties on canopy reflectance. Therefore, drawing from previous articles, 21 conventional VIs and 5 red-edge indices were selected as alternative features for constructing the FVC retrieval model (Table V).

Selecting appropriate VIs through feature selection methods is essential to improve the performance and efficiency of the FVC retrieval model. This article employs the tree-model-based feature selection method in ML algorithms, an approach widely used across various fields. The assessment of feature importance in tree node splits involves measuring the reduction in prediction result variance when features are included. By aggregating the variance reduction across all nodes of all trees, the overall contribution of each feature to the model is evaluated, representing the total impact of the VIs on the developed FVC retrieval model. Subsequently, the importance of all features is normalized to ensure that their sum equals 1, facilitating an accurate assessment of each feature's contribution to the retrieval capability of the model. Feature importance rankings (Fig. 5) were conducted on the 21 VIs calculated from the blue, green, red, and NIR bands, as well as on the 26 VIs calculated from

TABLE V
VIs CALCULATED FROM THE LESS DATASET

VIs	Description	Formula	Reference
NDVI	Normalized difference vegetation index	**(NIR-R)/(NIR+R)**	**[44]**
DVI	Difference vegetation index	NIR-R	[45]
EVI	Enhanced vegetation index	2.5*(NIR-R)/(NIR+6*R−7.5*B+1)	[46]
RVI	**Ratio vegetation index**	**R/NIR**	**[47]**
EVI2	Two-band enhanced vegetation index	2.5*(NIR-R)/(NIR+2.4*R+1)	[48]
RDVI	Renormalized difference vegetation index	$(NIR-R)/(NIR+R)^{0.5}$	[49]
GNDVI	**Green normalized difference vegetation index**	**(NIR-G)/(NIR+G)**	**[50]**
NIRv	Near-infrared reflectance of terrestrial vegetation	NDVI*NIR	[51]
OSAVI	Optimized soil-adjusted vegetation index	(NIR-R)/(NIR+R+0.16)	[52]
MSR	**Modified simple ratio**	$\mathbf{(NIR/R-1)/(NIR/R+1)^{0.5}}$	**[53]**
MNLI	**Modified nonlinear vegetation index**	$\mathbf{(NIR^2-R)(1+L)/(NIR^2+R+L)}$	**[54]**
MSAVI	Modified soil-adjusted vegetation index	$\{2*NIR+1-[(2*NIR+1)^2-8*(NIR-R)]^{0.5}\}/2$	[55]
CI	Chlorophyll index	NIR/G-1	[56]
SR	**Simple ratio**	**NIR/R**	**[57]**
TriVI	Triangular vegetation index	0.5*[120*(NIR-G)-200*(R-G)]	[58]
TDVI	Transformed difference vegetation index	$1.5*(NIR-R)/(NIR^2+R+0.5)^{0.5}$	[59]
SAVI	Soil-adjusted vegetation index	(1+L)(NIR−R)/(NIR+R+L)	[60]
NGRDI	Normalized green red difference index	(G−R)(G+R)	[61]
RCC	Red chromatic coordinate	R/(R+G+B)	[62]
RGBVI	**Red--green--blue vegetation index**	**$(G^2-B*R)/(G^2+B*R)$**	**[63]**
KNDVI	**Kernel normalized difference vegetation index**	**$TANH(NDVI^2)$**	**[64]**
NDRE	RedEdge normalized difference vegetation index	(NIR-RE)/(NIR+RE)	[65]
RERVI	**RedEdge ratio vegetation index**	**(RE-R)/(RE+R)**	**[66]**
REMSR	RedEdge modified simple ratio	$(NIR/RE-1)/(NIR/RE+1)^{0.5}$	[67]
RECI	RedEdge chlorophyll index	(NIR/RE)−1	[68]
LCI	Leaf chlorophyll index	(NIR-RE)/(NIR+R)	[66]

*R, G, B, NIR stand for red, green, blue, near infrared channels respectively. RE represent the RE1 channel of Sentinel-2 MSI and RE channel of HJ-2. The L value is set to 0.5 [69].

the blue, green, red, NIR, and red-edge bands, respectively. The VIs with contributions larger than 0.01 were considered sensitive to the FVC model (Section II-D-1), and were used as input features for RF, CNN, and CNN-TL. This selection aims to capture the dynamics of maize FVC throughout the entire growth stage, thereby enhancing the model's sensitivity to FVC retrieval. Specifically, MNVI, RVI, GNDVI, KNDVI, NDVI, RGBVI, SR, and MSR were used as input features when retrieving FVC using GF-1 data. MNVI, RVI, GNDVI, MSR, RGBVI, KNDVI, SR, NDVI, and RERVI were input features when estimating FVC from HJ-2 and Sentinel-2.

2) CNN: A CNN was pretrained using simulation data generated by a forward simulation process based on the LESS. Previous article has highlighted the potential of CNNs in remote sensing applications [70], [71]. The model development relies on PyTorch. For the pretraining process, the dataset generated from LESS simulation, containing 15 391 records, was split into a training dataset and a validation dataset at the 80% to 20% ratio. The optimizer used was Adam, with a learning rate set to 0.001 and a batch size of 64. The CNN pretraining process was commenced using the training dataset, where the data were input into the model and forward propagated to obtain prediction results. The loss between the retrieved and true values was calculated, and the loss values were accumulated. Subsequently, backpropagation was performed to update the parameters, and the R^2 and RMSE values over the validation set were recorded after each epoch of the training run. The mean absolute percentage error function was used as the loss function in this process

$$L = \frac{1}{n}\sum_{i=1}^{n}|y_i - y_i^p| \tag{1}$$

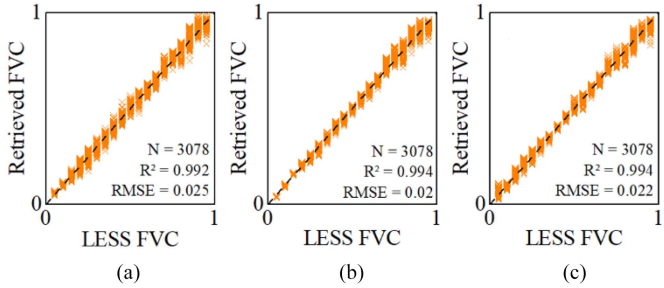

Fig. 6. Accuracy of theoretical simulations. Performance of the validation dataset of LD on CNN. (a) Resampled based on GF-1 SRF, (b) Resampled based on HJ-2 SRF, and (c) Resampled based on Sentinel-2 SRF.

where y_i and y_i^p represent the reference FVC and predicted FVC and n represents the size of the samples. After each epoch was completed, the validation dataset was used to validate the model. The article employs an early stopping method to prevent model overfitting, where the error on the validation set is calculated at the end of each epoch. If the error on the validation dataset begins to increase, the model training is stopped. The accuracy of the theoretical simulation is investigated using data generated from GF-1, HJ-2, and Sentinel-2 based on LESS simulation, and its validation dataset performs well on the pretrained model (Fig. 6). This adequately demonstrates the validity of LESS simulation and the suitability of CNN for FVC retrieval.

3) CNN–TL: The fully connected layers of the pretrained CNN structure were fine-tuned using GD, where the proportion of dataset division for fine-tuning and validating was 40% and 60%, respectively. For sufficient fine-tuning and validation, the splitting program was performed 50 times in the TL phase using different random seeds. The batch size was set at 8, and a smaller

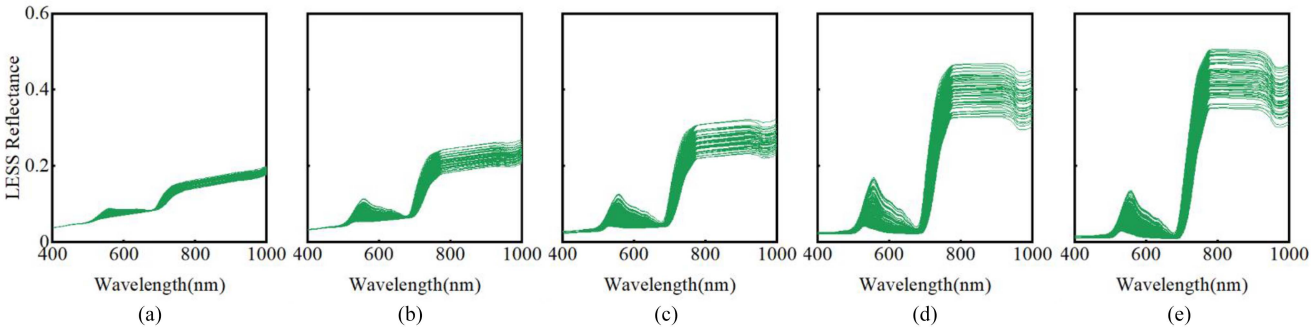

Fig. 7. Reflectance profiles of 400–1000 nm in maize canopy simulated by LESS with different parameter combinations at (a) FVC = 0.1, (b) FVC = 0.3, (c) FVC = 0.5, (d) FVC = 0.7, and (e) FVC = 0.9.

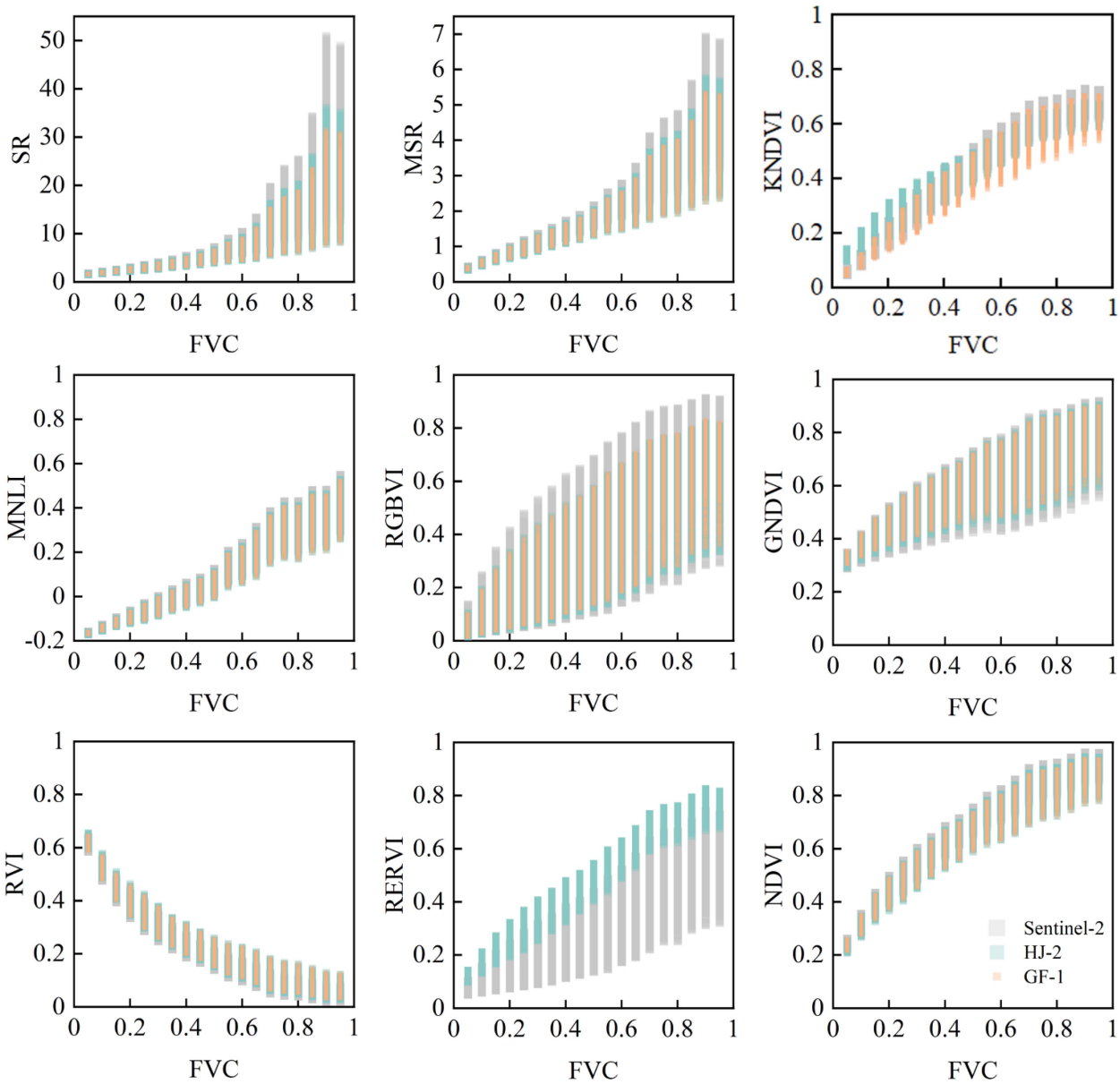

Fig. 8. Relationships of MNVI, RVI, NDVI, GNDVI, SR, MSR, RGBVI, KNDVI, and RERVI with FVC.

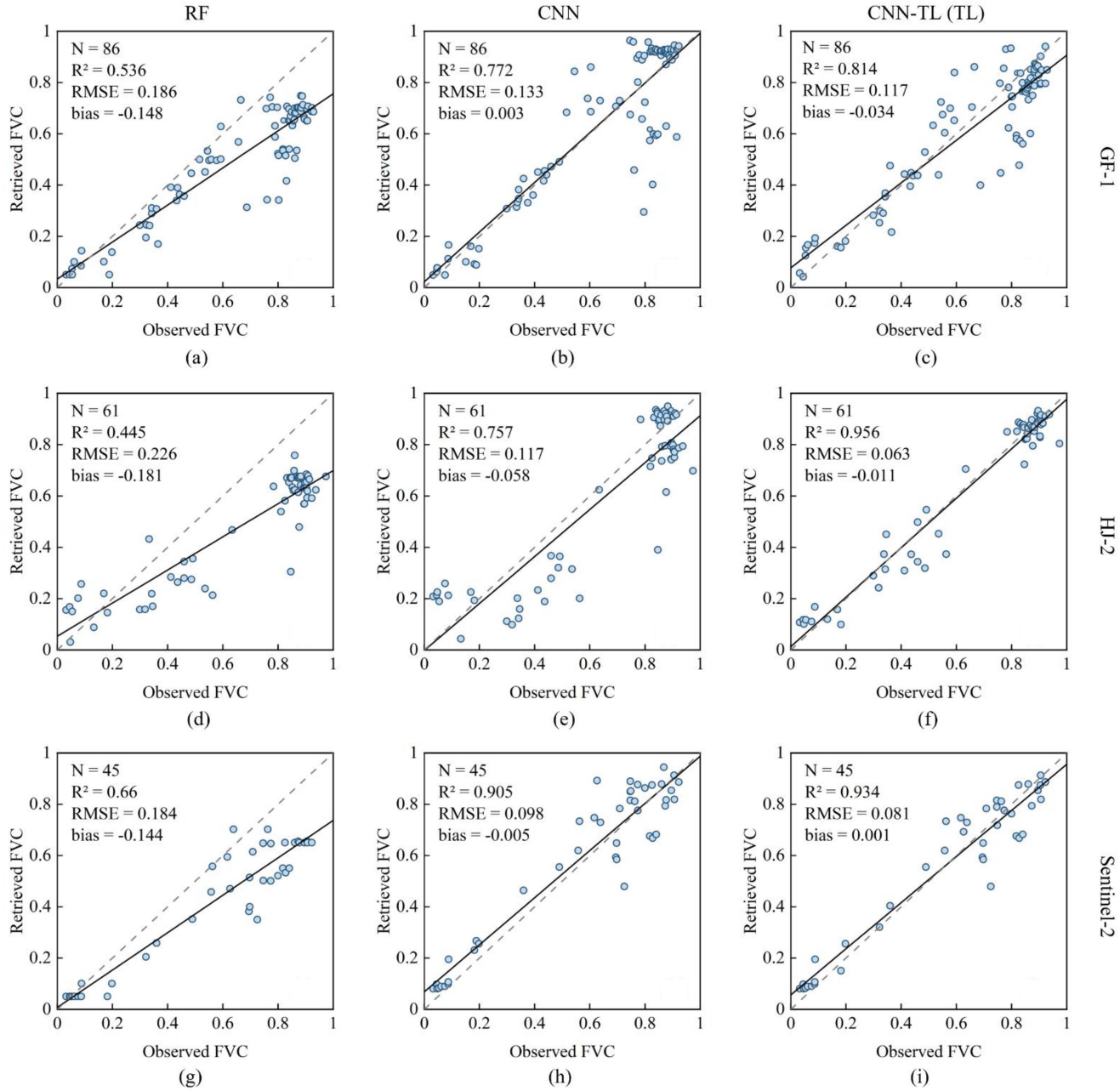

Fig. 9. Performance of RF, CNN, and CNN–TL on the validation dataset of GD: (a) GF-1-RF, (b) GF-1-CNN, (c) GF-1-TL, (d) HJ-2-RF, (e) HJ-2-CNN, (f) HJ-2-TL, (g) Sentinel-2-RF, (h) Sentinel-2-CNN, and (i) Sentinel-2-TL.

learning rate of 0.0001 was set in this phase since the model had already converged on the LESS simulation dataset. Other settings were the same as in the pretraining phase.

4) RF: The RF algorithm [72] trains several binary decision trees using the mean error and acquires the average from the leaf nodes of each tree. It employs the Bootstrap method to extract several samples from the original dataset and constructs a decision tree for each sample. The outputs of these decision trees are aggregated through simulation and iteration, and the final retrieval model is formed through a voting process. The RF algorithm shows high accuracy and wide applicability in vegetation parameter retrieval. In this article, the RF algorithm was used for comparison, and the dataset was used, refer to Table IV.

III. Results

A. Canopy Reflectance Simulated by LESS

Fig. 7 shows the canopy reflectance at different FVC levels simulated by LESS with different combinations of leaf properties, sun-sensor geometry, and soil background. The green peak caused by the strong reflection of chlorophyll appeared nearly at 550 nm. The strong absorption due to chlorophyll appeared at 680 nm, and the sharp increase happened at 700 to 780 nm which

is a typical red-edge phenomenon for green vegetation. The beginning of NIR region lied at 780 nm. The narrow absorption caused by water vapor was nearly 960 nm. The reflectance increased with the increase of FVC. We concluded that the LESS simulation framework was suitable for simulating the canopy spectral response of vegetation.

Fig. 8 shows the relationships between FVC and the VIs calculated from the simulated reflectance resampled by the SRF of GF-1, HJ-2, and Sentinel-2, respectively. The differences in VIs between GF-1 and HJ-2 were minimal because the two satellites sensors have similar spectral response (Fig. 4). The ranges of the eight VIs from GF-1 SRF show consistent with those from HJ-2. The KNDVI, MNLI, GNDVI, RVI, and NDVI values from Sentinel-2 were similar with those of GF-1 and HJ-2. However, SR and MSR from Sentinel-2 had higher values than those of GF-1 and HJ-2. The RGBVI from Sentinel-2 had a wider range than that of GF-1 and HJ-2 and the RERVI from Sentinel-2 was lower than that of HJ-2. Moreover, when FVC is close to 1, saturation of RVI and NDVI for three sensors was observed. The range of MSR and SR values became wider with the increase of FVC, which may lead to errors in retrieving high FVC values. Compared to the other VIs, GNDVI, RGBVI, and RERVI having larger ranges are sensitive to other canopy parameters, such as leaf area index and chlorophyll content. As a result, it makes sense to select different VIs to collaborate on developing the FVC retrieval model.

B. Performance of RF, CNN, and CNN–TL on Estimating Maize FVC From GF-1, HJ-2, and Sentinel-2

Nine FVC retrieval models were developed by using three different algorithms, RF, CNN, and CNN–TL, based on GF-1, HJ-2, and Sentinel-2 simulation reflectance, respectively. FVC were retrieved from GF-1, HJ-2, and Sentinel-2 imageries using the models and were validated by field FVC measurements (Fig. 9). It shows that RF had a moderate performance on three satellites datasets. The accuracy of RF at Sentinel-2 dataset ($R^2 = 0.66$, RMSE $= 0.184$, bias $= -0.144$) was higher than the other two satellite datasets. The FVC was underestimated at high canopy cover. Compared to RF models, CNN architecture improved the retrieval accuracy of FVC on the three satellite datasets. CNN achieved an accuracy of R^2 of 0.905 and RMSE of 0.098 on Sentinel-2 datasets and these values for GF-1 dataset were 0.772 and 0.133, higher than the accuracy obtained from HJ-2 dataset ($R^2 = 0.757$, RMSE $= 0.117$). After TL, the CNN model performance on GF-1, HJ-2, and Sentinel-2 all significantly improved, with the majority of the scatter plots lying close to the 1:1 line (Fig. 9). The CNN–TL had the best performance on HJ-2 dataset ($R^2 = 0.956$, RMSE $= 0.063$, bias $= -0.011$), followed by the CNN–TL on Sentinel-2 dataset ($R^2 = 0.934$, RMSE $= 0.081$, bias $= 0.001$). The retrieval accuracy of FVC from GF-1 was improved to 0.814 (R^2). It indicates that the use of TL helped the models perform better by utilizing LESS simulation knowledge. HJ-2 and Sentinel-2 outperformed GF-1. It is likely due to the red-edge band.

In order to comprehensively evaluate the modeling performance of RF, CNN, and CNN–TL on GF-1, HJ-2, and Sentinel-2, this article used the multiple statistics in Taylor's diagram to compare their ability to estimate FVC (Fig. 10). Although GF-1-CNN, HJ-2-CNN, and Sentinel-2-CNN were based on simulated data rather than field collected data, they all achieved an accuracy greater than 0.7. CNN–TL outperformed RF and CNN. HJ-2-TL and Sentinel-2-TL showed similar performance in terms of SD and RMSD, with HJ-2-TL having a higher correlation coefficient than Sentinel-2. However, GF-1-TL had a somewhat lower retrieval ability and a substantially higher SD than the HJ-2-TL and Sentinel-2-TL.

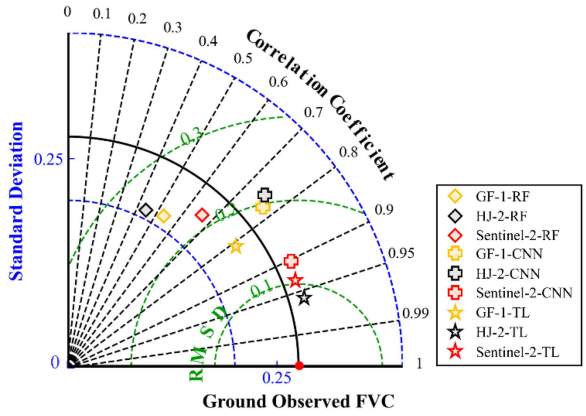

Fig. 10. Taylor diagrams compare the model performance of RF, CNN, and CNN–TL(TL) on GF-1, HJ-2, and Sentinel-2. The figure shows the correlation coefficient, SD, and RMSD in angular, radial, and concentric semicircular coordinates, respectively. The measured point indicates that the correlation coefficient is equal to 1 and the RMSD is equal to 0. Model retrieval performance is better when points are closer to the measurement point.

C. Mapping FVC From GF-1, HJ-2, and Sentinel-2 Based on CNN–TL

Fig. 11 depicts the spatial distributions of FVC estimated by CNN–TL from GF-1, HJ-2, and Sentinel-2 data in June 2022 and June 2023. It demonstrates that the FVCs retrieved by three satellites had a continuous spatial distribution throughout the study area. Fig. 12(a) shows the histograms of FVCs obtained by the three satellites in June 2022. The average FVC values for Sentinel-2 (green dashed line), HJ-2 (blue dashed line), and GF-1 (red dashed line) were 0.21, 0.25, and 0.11, respectively. In comparison, the FVC distributions obtained from GF-1 and HJ-2 were more similar. Fig. 12(b) shows the histogram of FVC for June 2023. The mean FVC values obtained from Sentinel-2, HJ-2, and GF-1 were 0.38, 0.4, and 0.45, respectively. These three satellites showed similar distribution of FVC, which demonstrates the robustness of CNN–TL and its generalization across different satellites.

IV. Discussion

A. The Potential of Combining LESS Model With Transfer Learning to Retrieve Maize FVC

To quantitatively retrieve surface parameters, a thorough comprehension of the transfer mechanisms of solar radiation to the surface is essential. Compared to 1-D RTM, 3-D RTM is able to

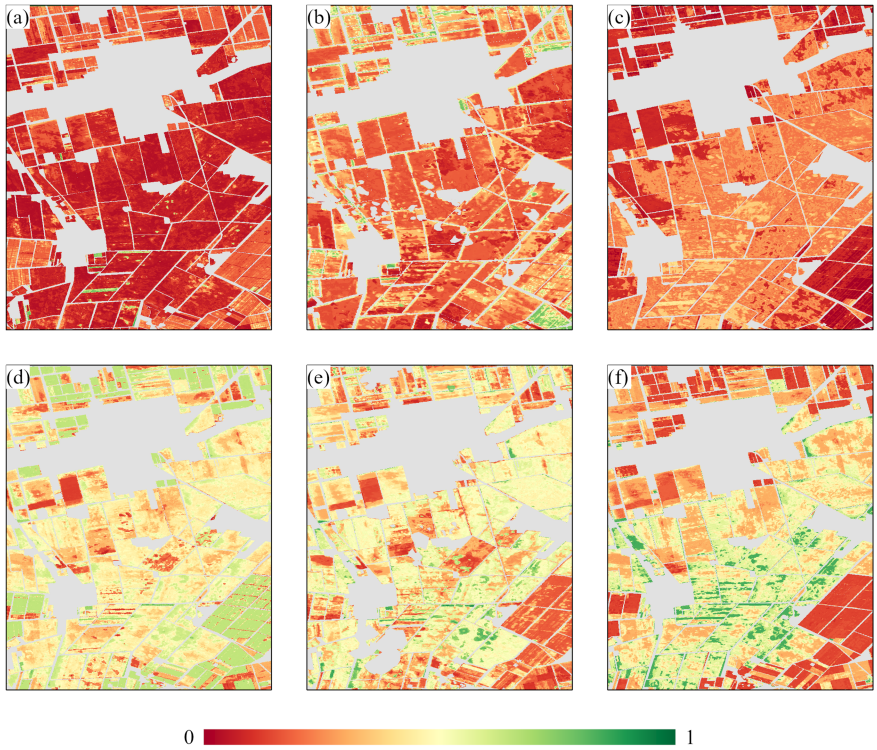

Fig. 11. FVC mapping using CNN–TL. Satellites and imaging dates are (a) GF-1, 2022/06/12, (b) HJ-2, 2022/06/10, (c) Sentinel-2, 2022/06/08, (d) GF-1, 2023/06/19, (e) HJ-2, 2023/06/19, and (f) Sentinel-2, 2023/06/18.

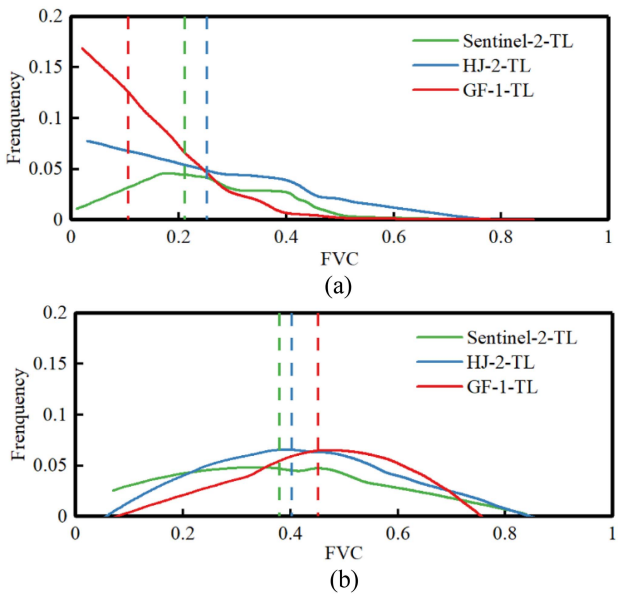

Fig. 12. Histogram of FVC retrieved from GF-1, HJ-2, and Sentinel-2 by CNN–TL: (a) in June 2022 and (b) in June 2023. Mean FVC values depicted by vertically dashed lines.

more accurately characterize the complexity of canopy structure. 3-D RTM is distinguished by its capacity to customize the scene and the elements, enabling precise simulation of the interaction between different sceneries and spectral components. Gao et al. [43] used LESS model to analyze the effect of crop structure types on VIs and noticed obvious difference in VIs between row structure and uniform structure. In this article, we used LESS model to characterize the row structure of maize at the initial phase of growth and the uniform structure at the late growth stage. To the best of our knowledge, it is the first time to concern the changes in maize structure. The superior retrieval accuracy of FVC by CNN–TL is partly due to the high precision of LESS in depicting the canopy structure. The application of LESS model can lead to a reduction in the need for man power to collect field data.

We obviously observed RF had an underestimation of high cover, which was consistent with the study of Sexton et al. [73] and DiMiceli et al. [74]. But this phenomenon was not observed in CNN and CNN–TL, which may be attributed to high learning efficiency of CNN and realistic constraints in model training. We used the entire pretrained model from LESS in the satellite-observed data space. For each sensor, the CNN–TL improved the model performance significantly compared to CNN and RF (Fig. 9). This finding aligned with prior article [35], [71]. It demonstrates that CNN–TL is effective and full of potential.

In addition, this article investigated the effect of field data size on CNN–TL. We conducted 20 comparative tests using randomly divided datasets. Each test contains a total of 100 field measured data. When using the amount of field data below 40%, the retrieval accuracy (R^2) of RF was lower than 0.5 (Fig. 13). When using more than 40% field data, RF tended to be stable. In contrast, CNN–TL exhibited superior stability against the different field sizes. TL offered significant benefits for FVC retrieval.

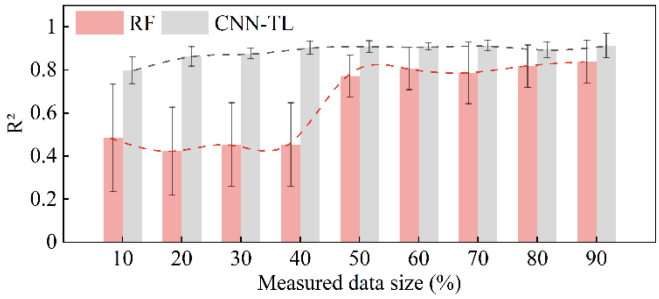

Fig. 13. Model performance of FVC retrieved with various measured data sizes. The error line is the standard deviation resulting from 20 random data splits.

B. Comparison of GF-1, HJ-2, and Sentinel-2 in Retrieving FVC

Because HJ-2 has just been launched, few research has used it to estimate FVC. The article validated and compared the performance of the proposed method on GF-1, HJ-2, and Sentinel-2 imageries. Although HJ-2 has only one red-edge band, it demonstrated equivalent performance in retrieving FVC to Senitnel-2 (Fig. 9). In addition, HJ-2 is far more accurate in estimating FVC than GF-1, even though the SRF of GF-1 is identical to that of HJ-2. This indicated the importance of red-edge band for estimating FVC. The FVC maps generated by GF-1 and HJ-2 exhibited a high level of consistency in the study area, demonstrating comparable levels of fine detail accuracy. Nevertheless, the FVC maps derived from Sentinel-2 showed some discrepancy to those derived from GF-1 and HJ-2 (Fig. 11). The increased spatial resolution of Sentinel-2 offers additional information, such as terrain and shading, which can lead to differences in the FVC maps when compared to GF-1 and HJ-2. HJ-2 has a temporal resolution of 2 days and GF-1 has a temporal resolution of 4 days. The combination of HJ-2, GF-1, and Sentinel-2 allow us to obtain more valuable information, reducing the disturbance of clouds, and ultimately improve data availability and accuracy.

To precisely assess FVC dynamics and work toward completely closing the difference between simulated and satellite reflectance, more field experiments should be designed. Our future article aims to produce FVC products with high accuracy by combining CNN–TL with RTM-based methods and detailed ground measurements. This will enable us to deliver more trustworthy data for agricultural decision-making.

V. Conclusion

This article proposes a novel maize FVC estimation method that combines the LESS 3-D RTM and TL based on CNN. The CNN model was fine-tuned using field-collected FVC and reflectance data from GF-1, HJ-2, and Sentinel-2 images. The CNN–TL model offers a promising solution for improving crop FVC estimation accuracy. Key findings include the following.

1) The LESS model offers a promising solution for simulating canopy reflectance with the advantage of depicting canopy structure.
2) CNN–TL exhibits superior performance compared to RF and CNN. CNN–TL achieved an R^2 of 0.956 and RMSE of 0.063 from HJ-2 dataset, higher than those obtained from GF-1 and Sentinel-2 datasets. This underscores the importance of utilizing simulated reflectance data in conjunction with TL.
3) The capacity of HJ-2 to estimate FVC is comparable to Sentinel-2. The combination of multisource multispectral satellites offers potential for precision agriculture and crop breeding applications.

In summary, this article highlights the potential of the LESS simulation and CNN–TL as a tool for improving FVC estimation. Further article can expand the application of our proposed method to other crops.

References

[1] T. R. Tenreiro, M. García-Vila, J. A. Gómez, J. A. Jiménez-Berni, and E. Fereres, "Using NDVI for the assessment of canopy cover in agricultural crops within modelling research," *Comput. Electron. Agriculture*, vol. 182, Mar. 2021, Art. no. 106038.

[2] Y. Li, K. Guan, G. D. Schnitkey, E. DeLucia, and B. Peng, "Excessive rainfall leads to maize yield loss of a comparable magnitude to extreme drought in the United States," *Glob. Change Biol.*, vol. 25, no. 7, pp. 2325–2337, Jul. 2019.

[3] Y. Tu, K. Jia, S. Liang, X. Wei, Y. Yao, and X. Zhang, "Fractional vegetation cover estimation in heterogeneous areas by combining a radiative transfer model and a dynamic vegetation model," *Int. J. Digit. Earth*, vol. 13, no. 4, pp. 487–503, Apr. 2020.

[4] S. Yang et al., "Accurate estimation of fractional vegetation cover for winter wheat by integrated unmanned aerial systems and satellite images," *Front. Plant Sci.*, vol. 14, Sep. 2023, Art. no. 1220137.

[5] L. Wan et al., "A model for phenotyping crop fractional vegetation cover using imagery from unmanned aerial vehicles," *J. Exp. Botany*, vol. 72, no. 13, pp. 4691–4707, 2021.

[6] Y. Xia, K. Guan, K. Copenhaver, and M. Wander, "Estimating cover crop biomass nitrogen credits with Sentinel-2 imagery and sites covariates," *Agronomy J.*, vol. 113, no. 2, pp. 1084–1101, Mar. 2021.

[7] M. J. Hill and J. P. Guerschman, "Global trends in vegetation fractional cover: Hotspots for change in bare soil and non-photosynthetic vegetation," *Agriculture, Ecosyst. Environ.*, vol. 324, Feb. 2022, Art. no. 107719.

[8] C. A. Martin, R. Proulx, M. Vellend, and L. Fahrig, "How the relationship between vegetation cover and land-cover variance constrains biodiversity in a human dominated world," *Landscape Ecol.*, vol. 36, no. 11, pp. 3097–3104, Nov. 2021.

[9] R. Yu, S. Li, B. Zhang, and H. Zhang, "A deep transfer learning method for estimating fractional vegetation cover of Sentinel-2 multispectral images," *IEEE Geosci. Remote Sens. Lett.*, vol. 19, 2022, Art. no. 6005605.

[10] L. Li et al., "Review of ground and aerial methods for vegetation cover fraction (fCover) and related quantities estimation: Definitions, advances, challenges, and future perspectives," *ISPRS J. Photogrammetry Remote Sens.*, vol. 199, pp. 133–156, May 2023.

[11] A. Zare and K. C. Ho, "Endmember variability in hyperspectral analysis: Addressing spectral variability during spectral unmixing," *IEEE Signal Process. Mag.*, vol. 31, no. 1, pp. 95–104, Jan. 2014.

[12] B. Somers, G. P. Asner, L. Tits, and P. Coppin, "Endmember variability in spectral mixture analysis: A review," *Remote Sens. Environ.*, vol. 115, no. 7, pp. 1603–1616, Jul. 2011.

[13] X. Mu, S. Huang, H. Ren, G. Yan, W. Song, and G. Ruan, "Validating GEOV1 fractional vegetation cover derived from coarse-resolution remote sensing images over croplands," *IEEE J. Sel. Topics Appl. Earth Observ. Remote Sens.*, vol. 8, no. 2, pp. 439–446, Feb. 2015.

[14] J. Zhao, J. Li, Q. Liu, B. Xu, X. Mu, and Y. Dong, "Generation of a 16 m/10-day fractional vegetation cover product over China based on Chinese GaoFen-1 observations: Method and validation," *Int. J. Digit. Earth*, vol. 16, no. 2, pp. 4229–4246, Dec. 2023.

[15] K. Jia et al., "Fractional vegetation cover estimation algorithm for Chinese GF-1 wide field view data," *Remote Sens. Environ.*, vol. 177, pp. 184–191, 2016, doi: 10.1016/j.rse.2016.02.019.

[16] Y. Niu, W. Han, H. Zhang, L. Zhang, and H. Chen, "Estimating fractional vegetation cover of maize under water stress from UAV multispectral imagery using machine learning algorithms," *Comput. Electron. Agriculture*, vol. 189, Oct. 2021, Art. no. 106414.

[17] N. Wang, Y. Guo, X. Wei, M. Zhou, H. Wang, and Y. Bai, "UAV-based remote sensing using visible and multispectral indices for the estimation of vegetation cover in an oasis of a desert," *Ecol. Indicators*, vol. 141, Aug. 2022, Art. no. 109155.

[18] B. Melville, A. Fisher, and A. Lucieer, "Ultra-high spatial resolution fractional vegetation cover from unmanned aerial multispectral imagery," *Int. J. Appl. Earth Observ. Geoinf.*, vol. 78, pp. 14–24, Jun. 2019.

[19] M. J. Hill, Q. Zhou, Q. Sun, C. B. Schaaf, and M. Palace, "Relationships between vegetation indices, fractional cover retrievals and the structure and composition of Brazilian Cerrado natural vegetation," *Int. J. Remote Sens.*, vol. 38, no. 3, pp. 874–905, Feb. 2017.

[20] H. Kimm et al., "Deriving high-spatiotemporal-resolution leaf area index for agroecosystems in the U.S. corn belt using planet labs CubeSat and STAIR fusion data," *Remote Sens. Environ.*, vol. 239, Mar. 2020, Art. no. 111615.

[21] J. Yue et al., "Hyperspectral-to-image transform and CNN transfer learning enhancing soybean LCC estimation," *Comput. Electron. Agriculture*, vol. 211, Aug. 2023, Art. no. 108011.

[22] L. Wittstruck, T. Jarmer, D. Trautz, and B. Waske, "Estimating LAI from winter wheat using UAV data and CNNs," *IEEE Geosci. Remote Sens. Lett.*, vol. 19, 2022, Art. no. 2503405.

[23] C. Yin et al., "Improving burn severity retrieval by integrating tree canopy cover into radiative transfer model simulation," *Remote Sens. Environ.*, vol. 236, Jan. 2020, Art. no. 111454.

[24] J. M. Fernández-Guisuraga et al., "Fractional vegetation cover ratio estimated from radiative transfer modeling outperforms spectral indices to assess fire severity in several Mediterranean plant communities," *Remote Sens. Environ.*, vol. 290, 2023, Art. no. 113542, doi: 10.1016/j.rse.2023.113542.

[25] W. Verhoef, "Light scattering by leaf layers with application to canopy reflectance modeling: The SAIL model," *Remote Sens. Environ.*, vol. 16, no. 2, pp. 125–141, Oct. 1984.

[26] J.-P. Gastellu-Etchegorry et al., "Discrete anisotropic radiative transfer (DART 5) for modeling airborne and satellite spectroradiometer and LIDAR acquisitions of natural and urban landscapes," *Remote Sens.*, vol. 7, no. 2, pp. 1667–1701, Feb. 2015.

[27] H. Huang, W. Qin, and Q. Liu, "RAPID: A radiosity applicable to porous individual objects for directional reflectance over complex vegetated scenes," *Remote Sens. Environ.*, vol. 132, pp. 221–237, May 2013.

[28] J. Qi et al., "LESS: Large-scale remote sensing data and image simulation framework over heterogeneous 3D scenes," *Remote Sens. Environ.*, vol. 221, pp. 695–706, Feb. 2019.

[29] W. Verhoef, "Earth observation modeling based on layer scattering matrices," *Remote Sens. Environ.*, vol. 17, no. 2, pp. 165–178, Apr. 1985.

[30] Y. Si, M. Schlerf, R. Zurita-Milla, A. Skidmore, and T. Wang, "Mapping spatio-temporal variation of grassland quantity and quality using MERIS data and the PROSAIL model," *Remote Sens. Environ.*, vol. 121, pp. 415–425, Jun. 2012.

[31] J. Qi, D. Xie, J. Jiang, and H. Huang, "3D radiative transfer modeling of structurally complex forest canopies through a lightweight boundary-based description of leaf clusters," *Remote Sens. Environ.*, vol. 283, Dec. 2022, Art. no. 113301.

[32] Q. Yuan et al., "Deep learning in environmental remote sensing: Achievements and challenges," *Remote Sens. Environ.*, vol. 241, May 2020, Art. no. 111716.

[33] Y. Ma, S. Chen, S. Ermon, and D. B. Lobell, "Transfer learning in environmental remote sensing," *Remote Sens. Environ.*, vol. 301, Feb. 2024, Art. no. 113924.

[34] J. Zhou et al., "A deep transfer learning framework for mapping high spatiotemporal resolution LAI," *ISPRS J. Photogrammetry Remote Sens.*, vol. 206, pp. 30–48, Dec. 2023.

[35] S. Wang et al., "Airborne hyperspectral imaging of cover crops through radiative transfer process-guided machine learning," *Remote Sens. Environ.*, vol. 285, 2023, Art. no. 113386.

[36] Q. Zhou, Q. Yu, J. Liu, W. Wu, and H. Tang, "Perspective of Chinese GF-1 high-resolution satellite data in agricultural remote sensing monitoring," *J. Integrative Agriculture*, vol. 16, no. 2, pp. 242–251, Feb. 2017.

[37] Z. Li et al., "In-orbit test of the polarized scanning atmospheric corrector (PSAC) onboard Chinese environmental protection and disaster monitoring satellite constellation HJ-2 A/B," *IEEE Trans. Geosci. Remote Sens.*, vol. 60, 2022, Art. no. 4108217.

[38] M. Drusch et al., "Sentinel-2: ESA's optical high-resolution mission for GMES operational services," *Remote Sens. Environ.*, vol. 120, pp. 25–36, May 2012.

[39] J. Cheng et al., "Estimating canopy-scale chlorophyll content in apple orchards using a 3D radiative transfer model and UAV multispectral imagery," *Comput. Electron. Agriculture*, vol. 202, Nov. 2022, Art. no. 107401.

[40] K. Yan et al., "Evaluation of the vegetation-index-based dimidiate pixel model for fractional vegetation cover estimation," *IEEE Trans. Geosci. Remote Sens.*, vol. 60, 2022, Art. no. 4400514.

[41] J.-B. Féret, A. A. Gitelson, S. D. Noble, and S. Jacquemoud, "PROSPECT-D: Towards modeling leaf optical properties through a complete lifecycle," *Remote Sens. Environ.*, vol. 193, pp. 204–215, May 2017.

[42] X. Huang, H. Guan, L. Bo, Z. Xu, and X. Mao, "Hyperspectral proximal sensing of leaf chlorophyll content of spring maize based on a hybrid of physically based modelling and ensemble stacking," *Comput. Electron. Agriculture*, vol. 208, May 2023, Art. no. 107745.

[43] S. Gao et al., "Evaluating the saturation effect of vegetation indices in forests using 3D radiative transfer simulations and satellite observations," *Remote Sens. Environ.*, vol. 295, Sep. 2023, Art. no. 113665.

[44] R. A. Muller and A. Buffington, "Real-time correction of atmospherically degraded telescope images through image sharpening," *J. Opt. Soc. Amer.*, vol. 64, no. 9, Sep. 1974, Art. no. 1200.

[45] A. J. Richardson, "Distinguishing vegetation from soil background information," *Photogrammetric Eng. Remote Sens.*, vol. 43, no. 12, pp. 1541–1552, Dec. 1977.

[46] A. Bannari, D. Morin, F. Bonn, and A. R. Huete, "A review of vegetation indices," *Remote Sens. Rev.*, vol. 13, no. 1/2, pp. 95–120, Aug. 1995.

[47] R. L. Pearson, "Remote mapping of standing crop biomass for estimation of the productivity of the shortgrass prairie," in *Proc. 8th Int. Symp. Remote Sens. Environ.*, 1972, pp. 1357–1381.

[48] Z. Jiang et al., "Analysis of NDVI and scaled difference vegetation index retrievals of vegetation fraction," *Remote Sens. Environ.*, vol. 101, no. 3, pp. 366–378, Apr. 2006.

[49] D. Haboudane, "Hyperspectral vegetation indices and novel algorithms for predicting green LAI of crop canopies: Modeling and validation in the context of precision agriculture," *Remote Sens. Environ.*, vol. 90, no. 3, pp. 337–352, Apr. 2004.

[50] A. A. Gitelson and M. N. Merzlyak, "Remote sensing of chlorophyll concentration in higher plant leaves," *Adv. Space Res.*, vol. 22, no. 5, pp. 689–692, Jan. 1998.

[51] G. Badgley, C. B. Field, and J. A. Berry, "Canopy near-infrared reflectance and terrestrial photosynthesis," *Sci. Adv.*, vol. 3, no. 3, Mar. 2017, Art. no. e1602244.

[52] A. R. Huete, "A soil-adjusted vegetation index (SAVI)," *Remote Sens. Environ.*, vol. 25, no. 3, pp. 295–309, Aug. 1988.

[53] J. M. Chen, "Evaluation of vegetation indices and a modified simple ratio for boreal applications," *Can. J. Remote Sens.*, vol. 22, no. 3, pp. 229–242, Sep. 1996.

[54] P. Gong, R. Pu, G. S. Biging, and M. R. Larrieu, "Estimation of forest leaf area index using vegetation indices derived from hyperion hyperspectral data," *IEEE Trans. Geosci. Remote Sens.*, vol. 41, no. 6, pp. 1355–1362, Jun. 2003.

[55] J. Qi, A. Chehbouni, A. R. Huete, Y. H. Kerr, and S. Sorooshian, "A modified soil adjusted vegetation index," *Remote Sens. Environ.*, vol. 48, no. 2, pp. 119–126, May 1994.

[56] A. A. Gitelson, Y. Gritz, and M. N. Merzlyak, "Relationships between leaf chlorophyll content and spectral reflectance and algorithms for non-destructive chlorophyll assessment in higher plant leaves," *J. Plant Physiol.*, vol. 160, no. 3, pp. 271–282, Jan. 2003.

[57] C. F. Jordan, "Derivation of leaf-area index from quality of light on the forest floor," *Ecology*, vol. 50, no. 4, pp. 663–666, Jul. 1969.

[58] N. H. Broge and E. Leblanc, "Comparing prediction power and stability of broadband and hyperspectral vegetation indices for estimation of green leaf area index and canopy chlorophyll density," *Remote Sens. Environ.*, vol. 76, no. 2, pp. 156–172, May 2001.

[59] A. Bannari, H. Asalhi, and P. M. Teillet, "Transformed difference vegetation index (TDVI) for vegetation cover mapping," in *Proc. IEEE Int. Geosci. Remote Sens. Symp.*, 2002, pp. 3053–3055.

[60] A. R. Huete, "A soil-adjusted vegetation index (SAVI)," *Remote Sens. Environ.*, vol. 25, no. 3, pp. 295–309, Aug. 1988.
[61] C. J. Tucker, "Red and photographic infrared linear combinations for monitoring vegetation," *Remote Sens. Environ.*, vol. 8, no. 2, pp. 127–150, May 1979.
[62] A. R. Gillespie, A. B. Kahle, and R. E. Walker, "Color enhancement of highly correlated images. II. Channel ratio and 'chromaticity' transformation techniques," *Remote Sens. Environ.*, vol. 22, no. 3, pp. 343–365, Aug. 1987.
[63] J. Bendig et al., "Combining UAV-based plant height from crop surface models, visible, and near infrared vegetation indices for biomass monitoring in barley," *Int. J. Appl. Earth Observ. Geoinf.*, vol. 39, pp. 79–87, Jul. 2015.
[64] G. Camps-Valls et al., "A unified vegetation index for quantifying the terrestrial biosphere," *Sci. Adv.*, vol. 7, no. 9, Feb. 2021, Art. no. eabc7447.
[65] A. Gitelson and M. N. Merzlyak, "Spectral reflectance changes associated with autumn senescence of aesculus hippocastanum L. and acer platanoides L. leaves. Spectral features and relation to chlorophyll estimation," *J. Plant Physiol.*, vol. 143, no. 3, pp. 286–292, Mar. 1994.
[66] Y. Zhu et al., "Exploring the potential of WorldView-2 red-edge band-based vegetation indices for estimation of mangrove leaf area index with machine learning algorithms," *Remote Sens.*, vol. 9, no. 10, Oct. 2017, Art. no. 1060.
[67] C. Wu, Z. Niu, Q. Tang, and W. Huang, "Estimating chlorophyll content from hyperspectral vegetation indices: Modeling and validation," *Agricultural Forest Meteorol.*, vol. 148, no. 8/9, pp. 1230–1241, Jul. 2008.
[68] A. A. Gitelson, G. P. Keydan, and M. N. Merzlyak, "Three-band model for noninvasive estimation of chlorophyll, carotenoids, and anthocyanin contents in higher plant leaves," *Geophys. Res. Lett.*, vol. 33, no. 11, Jun. 2006, Art. no. 2006GL026457.
[69] A. Nagy, J. Fehér, and J. Tamás, "Wheat and maize yield forecasting for the Tisza river catchment using MODIS NDVI time series and reported crop statistics," *Comput. Electron. Agriculture*, vol. 151, pp. 41–49, Aug. 2018.
[70] D. Jin, J. Qi, H. Huang, and L. Li, "Combining 3D radiative transfer model and convolutional neural network to accurately estimate forest canopy cover from very high-resolution satellite images," *IEEE J. Sel. Topics Appl. Earth Observ. Remote Sens.*, vol. 14, pp. 10953–10963, 2021.
[71] J. Yue et al., "Mapping cropland rice residue cover using a radiative transfer model and deep learning," *Comput. Electron. Agriculture*, vol. 215, Dec. 2023, Art. no. 108421.
[72] M. Belgiu and L. Drăguţ, "Random forest in remote sensing: A review of applications and future directions," *ISPRS J. Photogrammetry Remote Sens.*, vol. 114, pp. 24–31, Apr. 2016.
[73] J. O. Sexton et al., "Global, 30-m resolution continuous fields of tree cover: Landsat-based rescaling of MODIS vegetation continuous fields with LiDAR-based estimates of error," *Int. J. Digit. Earth*, vol. 6, no. 5, pp. 427–448, 2013.
[74] C. M. DiMiceli, M. L. Carroll, R. A. Sohlberg, C. Huang, M. C. Hansen, and J. R. G. Townshend, *Annual Global Automated MODIS Vegetation Continuous Fields (MOD44B) at 250 m Spatial Resolution for Data Years Beginning Day 65, 2000–2010 Collection 5 Percent Tree Cover*. College Park, MD, USA: Univ. Maryland, 2011.

Zhuo Wu is currently working toward the master's degree in cartography and geography information system with the Northeast Normal University, Changchun, China.

Her research interests include vegetation remote sensing and its application in agricultural research.

Xingming Zheng (Member, IEEE) received the Ph.D. degree in cartography and geographic information system from the Northeast Institute of Geography and Agroecology, Chinese Academy of Sciences, Changchun, China, in 2012.

Since 2012, he is a Research Associate with the Northeast Institute of Geography and Agroecology, Chinese Academy of Sciences. His research interests include passive microwave remote sensing of soil moisture, geophysical inversion model, microwave radiative/scattering transfer model, and its application on crop canopy.

Yanling Ding (Member, IEEE) received the Ph.D. degree in cartography and geographic information system from the Northeast Institute of Geography and Agroecology, Chinese Academy of Sciences, Changchun, China, in 2015.

She is currently an Associate Professor with the School of Geographical Sciences, Northeast Normal University, Changchun. Her research interests include optical remote sensing of photosynthetic vegetation and nonphotosynthetic vegetation and remote sensing application in agriculture.

Zui Tao was born in China, in 1984. He received the B.S. degree from the Henan University, Kaifeng, China, in 2005, the M.S. degree from the Wuhan University, Wuhan, China, in 2008, and the Ph.D. degree from the Institute of Remote Sensing and Digital Earth, Chinese Academy of Sciences (CAS), Beijing, China, in 2012, all in cartography and geographic information system.

He is currently a Research Assistant with the Aerospace Information Research Institute, CAS. His research interests include validation of remote sensing product, ecological, and environmental remote sensing.

Yuan Sun received the Ph.D. degree in cartography and geographic information system from the Institute of Remote Sensing and Digital Earth, Chinese Academy of Sciences, Beijing, China, in 2011.

Her research interests include validation of remote sensing product, ecological, and environmental remote sensing.

Bingze Li is currently working toward the Ph.D. degree in agricultural biological environmental and energy engineering with the Jilin University, Changchun, China, and the Northeast Institute of Geography and Agroecology, Chinese Academy of Sciences, Beijing, China.

His research interests include crop parameter modeling, microwave radiative transfer model improvement, and soil moisture sensor calibration.

Xinmeng Chen is currently working toward the master's degree in cartography and geography information system with the Northeast Normal University, Changchun, China.

Her research interests include estimation of nonphotosynthetic vegetation coverage.

Jianing Zhao received the bachelor's degree in geographic information science from the Northeast Forestry University, Harbin, China, in 2022. She is currently working toward the master's degree in cartography and geography information system with the Northeast Normal University, Changchun, China.

Her research interests include vegetation remote sensing and its application in agricultural research.

Yirui Liu received the bachelor's degree in geographic information science from the Hebei Normal University, Shijiazhuang, China, in 2023. She is currently working toward the master's degree in cartography and geographic information systems with the School of Geographical Sciences, Northeast Normal University, Changchun, China.

Xinyu Chen received the bachelor's degree in surveying and mapping engineering in 2021 from the Jilin Jianzhu University, Jinlin, China, where she is currently working toward the master's degree in cartography and geographic information engineering.

Her research interests include geographical information systems and the application of climate production potential in agriculture.

Xinbiao Li is currently working toward the master's degree in surveying and mapping engineering with the Jilin Jianzhu University, Changchun, China, and the Northeast Institute of Geography and Agroecology, Chinese Academy of Sciences, Beijing, China.

His research interests include impact of flood and drought disasters on farmland.